

# FLOW OVER A LOCALIZED HEAT SOURCE

M. A. ESTOQUE and C. M. BHUMRAKAR

University of Miami, Coral Gables, Fla.

## ABSTRACT

A general theoretical model has been designed to analyze the properties of perturbations induced when air flows over an isolated warm portion of the earth's surface. The dependence of these perturbations on wind and temperature conditions of the large-scale flow as well as on the orientation of the local heat source with respect to the prevailing flow has been examined by performing two numerical integrations. The heat source is considered to be narrow (10 km) in the  $x$ -direction and infinite in the  $y$ -direction.

The computations show that when the prevailing flow is strong, and normal to the heat source, the induced perturbations are weak. The surface wind over the heat source is accelerated and the wind at the leeward edge is stronger than at the windward side. Consequently, there is downward motion over the entire extent of the heat source. The corresponding results for the case when the prevailing flow is parallel to the heat source show considerably stronger induced perturbations and the heat source is characterized by upward motions.

## 1. INTRODUCTION

When air flows over an isolated warm portion of the earth's surface, its properties are altered by the addition of heat from the underlying surface. Heat is transported from the surface to the lowest atmospheric layers by molecular and small-scale eddy diffusion. The heat in these layers is, in turn, transported to upper levels by penetrative convection and the ensuing larger scale circulations. Under favorable conditions, precipitation may occur and release the latent heat of condensation. This additional heating leads to the development of vigorous perturbations. It is obvious that the properties of the induced perturbations depend mainly on the following factors:

- 1) the wind, temperature, and moisture conditions of the large-scale flow and
- 2) the horizontal extent, shape, and intensity of the local heat source and its orientation with respect to the prevailing flow. This paper describes a general model designed to analyze this dependence.

Theoretical studies of the flow over localized heat sources have been made by Malkus and Stern (1953), Stern and Malkus (1953), and Smith (1955, 1957). In both their joint studies, Malkus and Stern integrated steady-state models. Smith, on the other hand, used time-dependent models. There are two important shortcomings of the foregoing studies. These are the use of the linearization assumption and a somewhat crude specification of the heating function. We have attempted to remedy these shortcomings in our present model, which incorporates the effects of surface boundary layer processes and penetrative convection. The model equations will be described, and two examples of the results of an integration will be discussed in the following sections. The important effects of heating and cooling due to condensation and evaporation of water are incorporated in a more general model which will form the subject of a forthcoming paper.

## 2. BASIC EQUATIONS

The equations have been formulated using a right-handed rectangular system (fig. 1) with the origin at the midpoint of the heat source, which is considered to be infinitely long along the  $y$ -direction; the motion and temperature are assumed to be constant along this direction. We have neglected the local time derivative of density in the equation of continuity and have assumed the motion to be hydrostatic.

On the basis of above assumptions, the meteorological equations may be written as

$$\frac{\partial u}{\partial t} = -u \frac{\partial u}{\partial x} - w \frac{\partial u}{\partial z} + fv - \frac{1}{\rho_s} \frac{\partial p}{\partial x} + \frac{\partial}{\partial z} \left( K_z \frac{\partial u}{\partial z} \right) + \left( \frac{\partial u}{\partial t} \right)_{pc} + K_H \frac{\partial^2 u}{\partial x^2}, \quad (1)$$

$$\frac{\partial v}{\partial t} = -u \frac{\partial v}{\partial x} - w \frac{\partial v}{\partial z} + f(u_s - u) + \frac{\partial}{\partial z} \left( K_z \frac{\partial v}{\partial z} \right) + \left( \frac{\partial v}{\partial t} \right)_{pc} + K_H \frac{\partial^2 v}{\partial x^2}, \quad (2)$$

$$\frac{\partial}{\partial z} \left( \frac{p}{\rho_0} \right)^{R/c_p} = -\frac{g}{c_p \theta}, \quad (3)$$

$$\frac{\partial}{\partial x} (\rho_s u) + \frac{\partial}{\partial z} (\rho_s w) = 0, \quad (4)$$

$$\frac{\partial \theta}{\partial t} = -u \frac{\partial \theta}{\partial x} - w \frac{\partial \theta}{\partial z} + \frac{\partial}{\partial z} \left( K_z \frac{\partial \theta}{\partial z} \right) + \left( \frac{\partial \theta}{\partial t} \right)_{pc} + K_H \frac{\partial^2 \theta}{\partial x^2}, \quad (5)$$

$$p = \rho RT \quad (6)$$

and

$$\frac{\theta}{T} = \left( \frac{p_0}{p} \right)^{R/c_p}. \quad (7)$$

The variables are in customary notation. Equations (1) to (3) are the equations of motion along the  $x$ ,  $y$ , and  $z$ , respectively. Equation (4) is the equation of continuity.

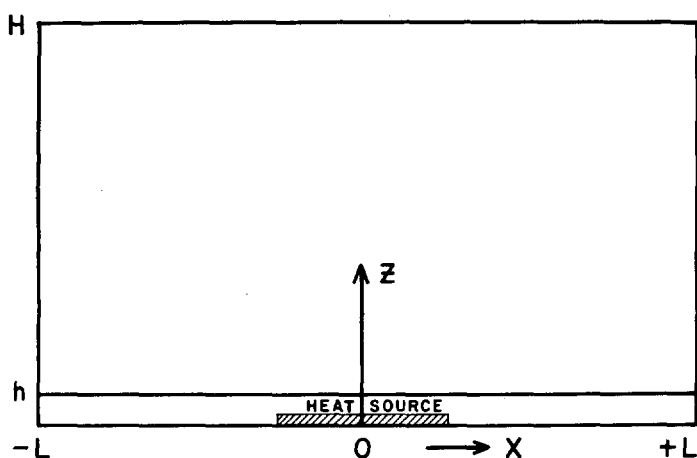


FIGURE 1.—The coordinate system.

Equation (5) is the thermodynamic energy equation. Equations (6) and (7) are, respectively, the equations of state and the Poisson equation. The terms with the subscript  $pc$ , which represent the effect of vertical mixing by penetrative convection, have been computed using formulas described by Estoque (1968). The quantity  $u_g$  represents the pressure gradient force along the  $y$ -direction; in the computations it is specified as an arbitrary function of height. The subscript  $s$  in the density indicates the value of density for the standard atmosphere. The seven unknown variables ( $u, v, w, \theta, p, T, \rho$ ) are to be determined as functions of  $x, z$ , and  $t$  in the region shown in figure 1. The solutions are obtained by numerical integration.

### 3. THE GRID AND THE BOUNDARY AND INITIAL CONDITIONS

The grid network consists of 31 points along  $x$  and 17 points along  $z$ . The grid spacing is variable (table 1) and is specified in such a way that high resolution is achieved at lower levels and also in the vicinity of the heat source. The finite-difference equations are based on forward time and upstream uncentered space differences.

The lateral boundaries of the region of integration are at  $x = -105$  km and 105 km. The lower and the upper boundaries are located at  $z = 0$  and 12 km. The local heat source at the surface is specified by prescribing higher temperature over a central portion of the lower boundary than the outer portions.

In our calculations the local heat source is  $10^\circ\text{C}$  warmer than surroundings. This temperature excess is greater than that used by Malkus (1963). However, it corresponds well with that reported by Black (1963), whose experiments showed that asphalt-coated soils attain more than  $10^\circ\text{C}$  advantage over the surroundings near midday. The important boundary conditions are summarized below.

TABLE 1.—Grid spacing for a localized heat source. Height  $z$  above the surface for the height index  $j$ , and distance  $x$  from the center of the heat source for the horizontal index  $i$ 

$j$	$z$ (m)	$i$	$x$ (km)	$i$	$x$ (km)
1	0.0	1	-105.0	17	1.0
2	1.8	2	-40.3	18	2.0
3	4.5	3	-34.2	19	3.0
4	12	4	-28.5	20	4.0
5	32	5	-23.3	21	5.0
6	80	6	-18.6	22	6.0
7	210	7	-14.5	23	8.1
8	347	8	-10.9	24	10.9
9	524	9	-8.1	25	14.5
10	730	10	-6.0	26	18.6
11	964	11	-5.0	27	23.3
12	1545	12	-4.0	28	28.5
13	2100	13	-3.0	29	34.2
14	3171	14	-2.0	30	40.3
15	5870	15	-1.0	31	105.0
16	9647	16	0.0		
17	12353				

At  $z=0$  (bottom)—

$$u=v=w=0,$$

$$\theta=300^\circ\text{A for } -105 \text{ km} \leq x < -5 \text{ km},$$

$$\theta=310^\circ\text{A for } -5 \text{ km} \leq x \leq 5 \text{ km}, \text{ and}$$

$$\theta=300^\circ\text{A for } 5 \text{ km} < x \leq 105 \text{ km}.$$

At  $z=12$  km (top)—

$$u=u_g; v=w=0; \theta=319^\circ\text{A}.$$

At all the inflow points on the lateral boundaries, the variables  $u, v$ , and  $\theta$  are assumed to be uniform along  $x$ . At the outflow points, the differencing scheme does not require boundary values for these variables. As regards the pressure computations (described in the next section) we need to prescribe the pressure only at the top of the lateral boundaries  $x = \pm 105$  km. This value of pressure, used in the present computations, corresponds to that of the standard atmosphere.

At the initial time, the wind is assumed to be in geostrophic equilibrium. The corresponding temperature field is computed from the wind using the thermal wind equation.

### 4. COMPUTATION OF PRESSURE

The pressure computation is based on equations (1), (3), and (4). We will describe how these equations are used in calculating the pressure field  $p$  when the temperature and the velocity distributions are given.

Differentiating equation (1) with respect to  $x$  and then averaging vertically from  $z=0$  to  $z=H$ , one gets

$$\frac{\partial^2 \bar{p}}{\partial x^2} = -\frac{\partial}{\partial x} (\rho_s G) \quad (9)$$

where

$$G = u \frac{\partial u}{\partial x} + w \frac{\partial u}{\partial z} - f v - \frac{\partial}{\partial z} \left( k_z \frac{\partial u}{\partial z} \right) - \left( \frac{\partial u}{\partial t} \right)_{pc} - K_H \frac{\partial^2 u}{\partial x^2}$$

and the bar operator represents the vertical average.

Also, integrating by parts and using the hydrostatic equation one gets the identity

$$\int_0^H p dz = \bar{p}H = pz|_0^H + \frac{g}{R} \int_0^H z \frac{p}{\theta} \left(\frac{p_0}{p}\right)^{R/c_p} dz$$

or

$$p_H = \bar{p} - \frac{g}{RH} \int_0^H z \frac{p}{\theta} \left(\frac{p_0}{p}\right)^{R/c_p} dz \quad (10)$$

where  $p_H$  is the value of pressure at  $z=12$  km. Equations (9) and (10) can be used in solving for the distribution of  $\bar{p}$  and  $p_H$ , respectively, in the interval  $-105 \text{ km} < x < 105 \text{ km}$ . The value of  $p_H$  thus obtained is then used in conjunction with the potential temperature and the hydrostatic equation to obtain the pressure distribution. For integrating equation (9), we specify the values of  $\bar{p}$  at the lateral boundaries. These values of  $\bar{p}$  are obtained by solving equation (10) for prescribed values of  $p_H$  at  $x = \pm 105 \text{ km}$ .

### 5. BOUNDARY LAYER EQUATIONS

In order to model the diffusion processes in the surface layers,  $0 \leq z \leq h$ , we introduce the following profile equations

$$U(z) = \frac{U_*}{k_0} \left[ \ln \frac{z+z_0}{z_0} + \frac{\alpha g}{\theta} \frac{\theta_*}{U_*} z^{1/2} \right] \quad (11)$$

and

$$\theta(z) = \theta_0 + \frac{\theta_*}{k_0} \left[ \ln \frac{z+z_0}{z_0} + \frac{\alpha g}{\theta} \frac{\theta_*}{U_*} z^{1/2} \right] \quad (12)$$

where  $z_0$  is the roughness parameter and  $k_0$  is the von Kármán constant;  $U_*$  and  $\theta_*$  are, respectively, the friction velocity and temperature.

The quantity  $U$  is the horizontal wind speed while  $\alpha$  is an empirical constant. These expressions incorporate the effect of thermal stratification somewhat differently from the so-called *KEYPS* formula mentioned by Lumley and Panofsky (1964). According to Clayton (1967), they appear to fit empirical data better over a wider range of thermally unstable stratification; he suggests a value of 18 for  $\alpha$ . In our computations, we have used a value of 1 cm for the roughness parameter. This choice of roughness parameter is arbitrary since we have not considered the effect of variations in the surface roughness in our model. The profile equations are used in the integrations as follows:

1) Using the initial value of  $u$ ,  $v$ , and  $\theta$  at  $z=h$  and the corresponding boundary values at  $z=0$ , we computed  $U_*$  and  $\theta_*$  with the aid of the profile equations (11) and (12).

2) The momentum and heat fluxes are calculated from  $U_*$  and  $\theta_*$ .

3) The vertical diffusion terms in equations (1) to (4) at  $z=h$ , are deduced from these fluxes and the corresponding fluxes in the layer bounded below by  $z=h$  and above by the next grid point. The latter flux is computed using finite differences.

4) The vertical diffusion terms at subsequent times are computed by repeating steps 1) to 4), except that now the latest predicted values of  $u$ ,  $v$ , and  $\theta$  are used in step 1).

### 6. THE DIFFUSION COEFFICIENTS

The formula for the vertical eddy diffusion coefficient  $K_z$  is

$$K_z = \begin{cases} l^2 \frac{\partial U}{\partial z} (1 - \alpha S) & \text{for } \frac{\partial \theta}{\partial z} < 0 \\ l^2 \frac{\partial U}{\partial z} (1 + \alpha S)^{-1} & \text{for } \frac{\partial \theta}{\partial z} > 0 \end{cases} \quad (13)$$

where

$$l = k_0(z+z_0) \left[ 1 + \frac{f(z+z_0) k_0}{27 \times 10^{-5} U_{(z=h)}} \right]^{-1}$$

and

$$S = \frac{(gl)^{1/2}}{\theta} \frac{\partial \theta / \partial z}{|\partial U / \partial z|}$$

It has been formulated by generalizing an expression due to Blackadar (1962) so that it incorporates a stability factor. The form of this factor is based on the profile equations (11) and (12) of the preceding section.

The horizontal eddy coefficient has been assumed to be constant ( $K_H = 10^8 \text{ cm}^2 \text{ sec}^{-1}$ ) in our integrations. In future work, however, we will specify it in terms of a larger scale velocity field following an idea suggested by Lilly (1968).

### 7. TWO EXAMPLES OF A NUMERICAL INTEGRATION

In order to test the realism of the theoretical model, we have integrated the equations for two cases. Case *a* simulates the evolution of the perturbation which occurs when the wind is initially geostrophic and normal to the central heated strip; case *b* simulates that which occurs when the initial flow is parallel to the strip. In both cases, the speed of the initial flow is assumed to be constant with height and is equal to  $10 \text{ m sec}^{-1}$ . The initial potential temperature distribution (uniform along the horizontal) is the same as that of the standard atmosphere. The integrations were made for a period of approximately 3 hr of meteorological time. At the end of the period, the velocity and temperature fields reached quasi-steady state conditions. The condition may be considered to represent the actual atmosphere of the early afternoon in the vicinity of an island surrounded by a colder ocean.

*Normal flow case (a)*—The development of the perturbations with time is indicated in figures 2 to 16 which show the velocity and temperature fields at  $t=15 \text{ min}$ ,  $30 \text{ min}$ ,  $1, 2$ , and  $3 \text{ hr}$  after the initial time. The isolines for all quantities represent the excesses over the corresponding values (at the same level) at the upstream boundary.

At  $t=15 \text{ min}$  (fig. 2), two separate circulation cells are seen, one over each edge of the central strip. The cells develop in response to the strong solenoidal field at these two points. The double cell pattern gradually

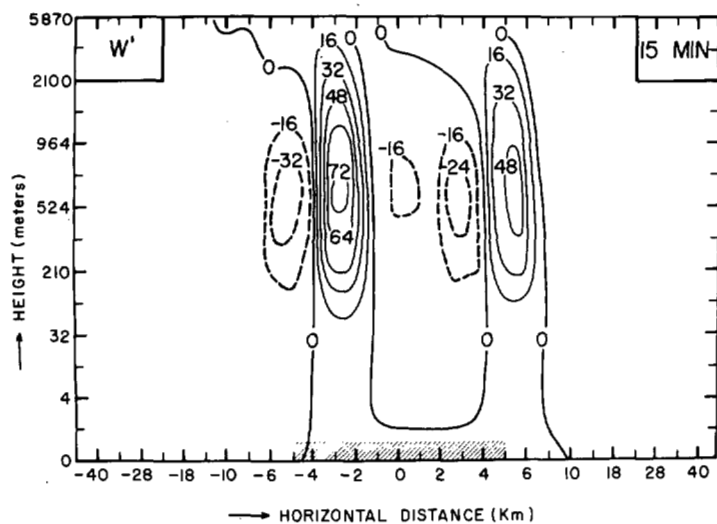


FIGURE 2.—Distribution of the vertical perturbation velocity  $w'$  ( $\text{cm sec}^{-1}$ ) at 15 min for case  $a$  when the initial prevailing flow is normal to the heat source.

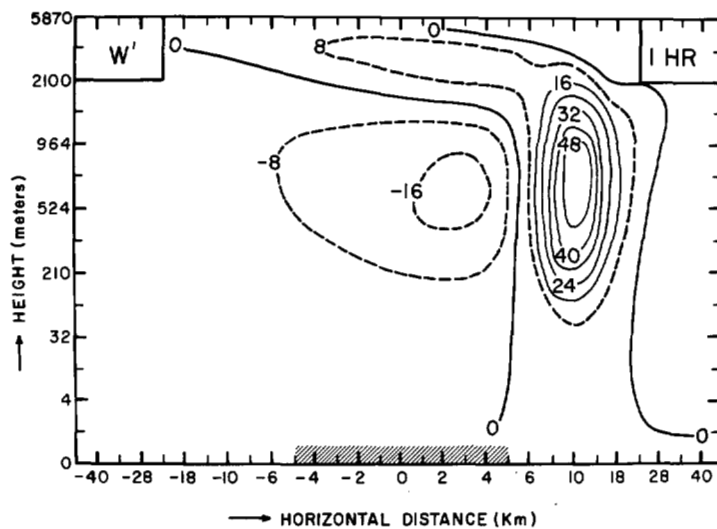


FIGURE 4.—Distribution of the vertical perturbation velocity  $w'$  ( $\text{cm sec}^{-1}$ ) at 1 hr for case  $a$  when the initial prevailing flow is normal to the heat source.

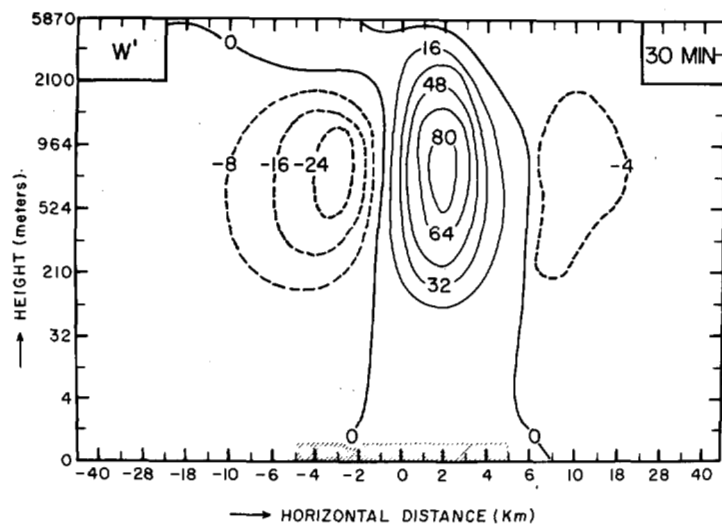


FIGURE 3.—Distribution of the vertical perturbation velocity  $w'$  ( $\text{cm sec}^{-1}$ ) at 30 min for case  $a$  when the initial prevailing flow is normal to the heat source.

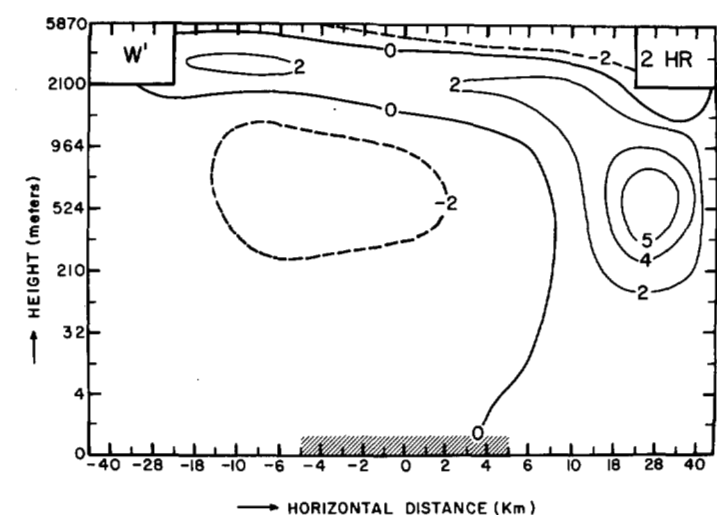


FIGURE 5.—Distribution of the vertical perturbation velocity  $w'$  ( $\text{cm sec}^{-1}$ ) at 2 hr for case  $a$  when the initial prevailing flow is normal to the heat source.

changes into that of a single cell as the leeward cell drifts downstream over the colder outskirts and then dissipates while the windward cell intensifies. The resulting single cell continues to move downstream; at the same time it decreases in intensity and expands in horizontal extent. During this period, the evolving temperature structure shows some interesting features. In the initial stages, strong upward heat transport by penetrative convection results in the warming of a deep layer of the atmosphere over the edges of the heated strip. This is indicated by the plumelike configuration of the isotherms in figure 7. Subsequently, the plume becomes tilted, and its top is eventually sheared off by the stronger winds at upper levels.

The approximately steady-state patterns (figs. 6, 11, and 16) reveal some significant features. Looking first at the vertical motion field (fig. 6), one is impressed by the predominance of downward motions over the entire extent of the warm strip as well as the region upwind. The maximum downward velocity component of  $2.0 \text{ cm sec}^{-1}$  is located directly over the windward edge at a height of  $0.5 \text{ km}$ . Upward motion prevails downwind of the warm central strip, including an area which extends as far as  $100 \text{ km}$  away. This pattern of vertical motions would result in clear skies over the heat source and cloudy conditions downwind.

The corresponding distribution of the horizontal perturbation velocity ( $u'$ ) normal to the heat source (fig. 16)

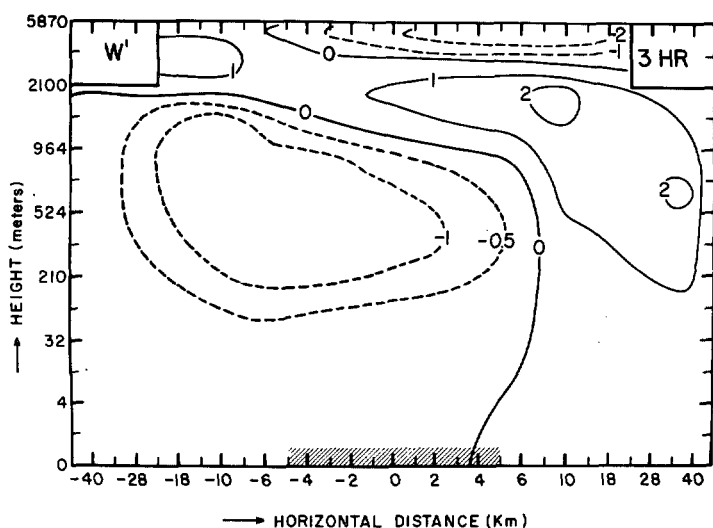


FIGURE 6.—Distribution of the vertical perturbation velocity  $w'$  ( $\text{cm sec}^{-1}$ ) at 3 hr for case  $a$  when the initial prevailing flow is normal to the heat source.

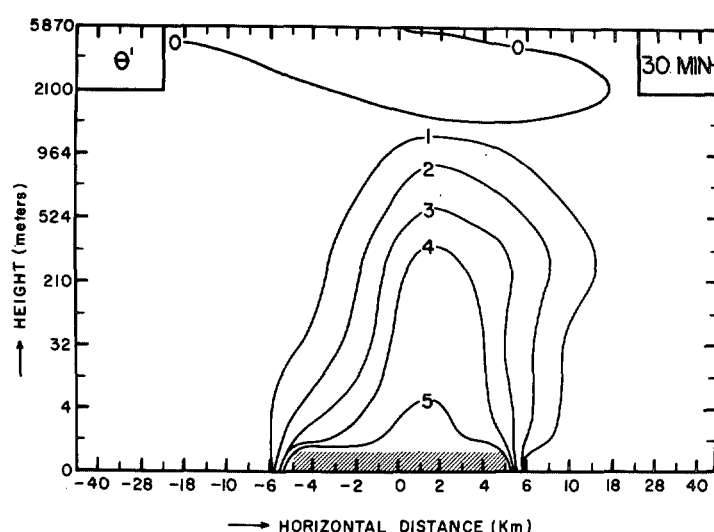


FIGURE 8.—Distribution of perturbation  $\theta'$  in potential temperature ( $^{\circ}\text{C}$ ) at 30 min for case  $a$  when the initial prevailing flow is normal to the heat source.

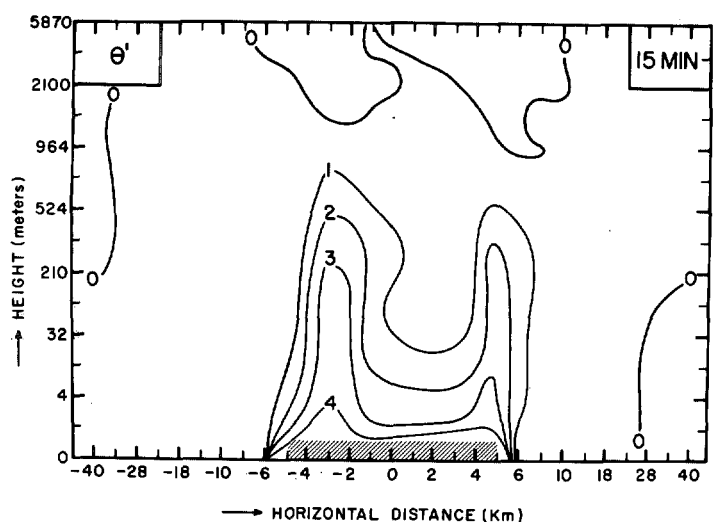


FIGURE 7.—Distribution of perturbation  $\theta'$  in potential temperature ( $^{\circ}\text{C}$ ) at 15 min for case  $a$  when the initial prevailing flow is normal to the heat source.

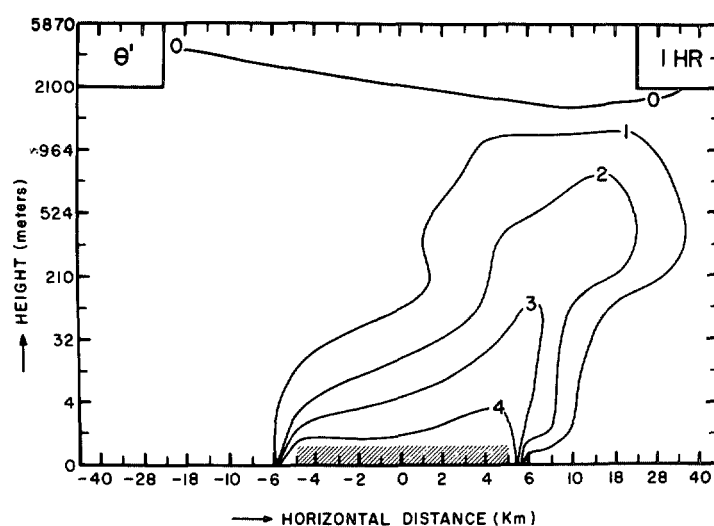


FIGURE 9.—Distribution of perturbation  $\theta'$  in potential temperature ( $^{\circ}\text{C}$ ) at 1 hr for case  $a$  when the initial prevailing flow is normal to the heat source.

shows that the local heating produces an acceleration of the wind at low levels not only over the warm central strip but also many tens of kilometers toward both the leeward and the windward directions. A compensating deceleration occurs above. The maximum perturbation in the speed occurs over the leeward edge of the heat source. The location of this maximum is very surprising because it is entirely contrary to what one would expect on the basis of the sea-breeze effect, which ordinarily tends to produce inshore winds at both leeward and windward edges. This would mean negative perturbations in  $u'$  at the leeward side. The theoretical calculations predict exactly the opposite, giving a maximum value of  $u'$

equal to  $2.0 \text{ m sec}^{-1}$ . What is even more surprising is that this value is greater than the speed at the windward edge which again is opposite to the sense which the sea-breeze effect implies.

This unexpected theoretical result appears to be confirmed by wind observations at Barbados (Garstang, 1968). The observations in the early afternoon show that the surface wind speeds over the island are greater than those over the open ocean. The observed wind speed at the windward station is about  $70 \text{ cm sec}^{-1}$  faster on the average than the open ocean speed; the corresponding speed at the leeward side is  $170 \text{ cm sec}^{-1}$  faster than the ocean speed. Garstang explains the daytime acceleration

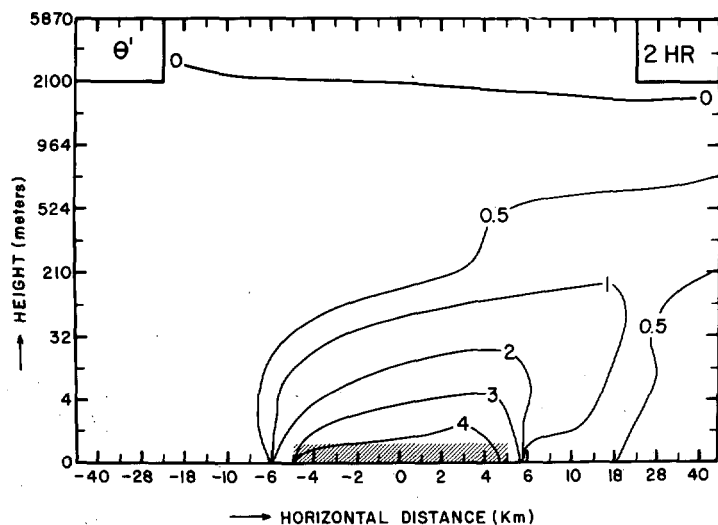


FIGURE 10.—Distribution of perturbation  $\theta'$  in potential temperature ( $^{\circ}\text{C}$ ) at 2 hr for case *a* when the initial prevailing flow is normal to the heat source.

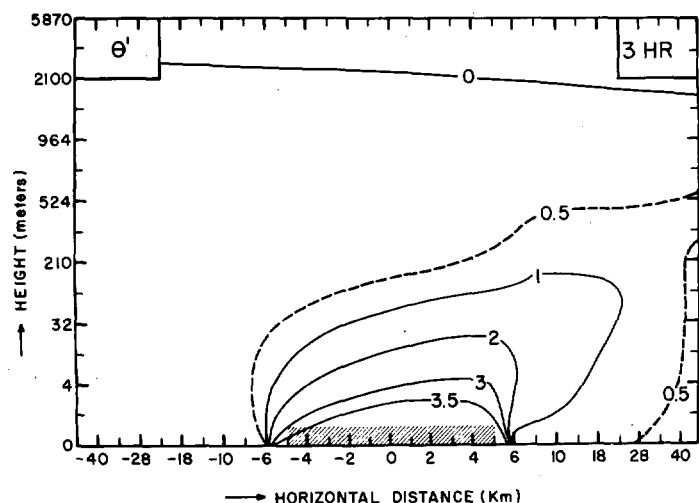


FIGURE 11.—Distribution of perturbation  $\theta'$  in potential temperature ( $^{\circ}\text{C}$ ) at 3 hr for case *a* when the initial prevailing flow is normal to the heat source.

over the island as a result of diurnal variations in the downward eddy transport of horizontal momentum associated with changes in the thermal stratification.

The results of our integration suggest an alternative explanation. It appears that the pressure gradient force and horizontal advective processes are more important than the eddy transport process. This may be deduced from table 2 that shows the magnitudes of the terms contributing to the local acceleration  $\partial u/\partial t$ . These have been computed for three locations, A, B, and C and for  $t=30$  min, 1, 1.5, 2, 2.5, and 3 hr. The points A and B are located at the windward and leeward edges, respectively; while the point C is about 10 km downwind of the leeward edge. All the three points are at a height of 80 m. It may be seen that, at both windward and leeward edges,

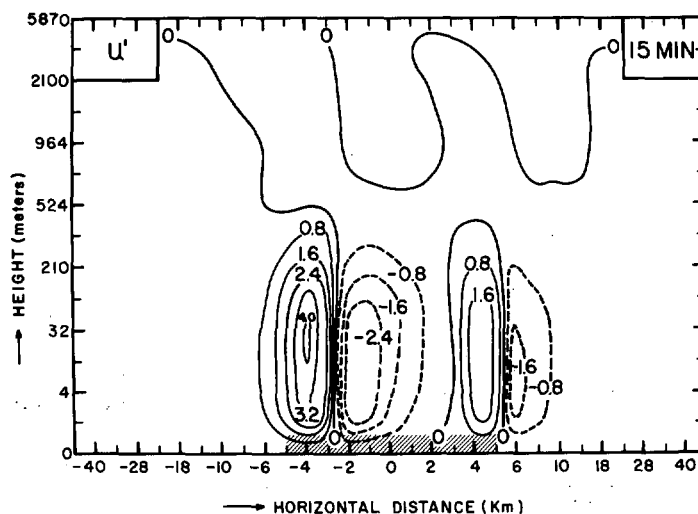


FIGURE 12.—Distribution of the horizontal perturbation velocity  $u'$  ( $\text{m sec}^{-1}$ ) at 15 min for case *a* when the initial prevailing flow is normal to the heat source.

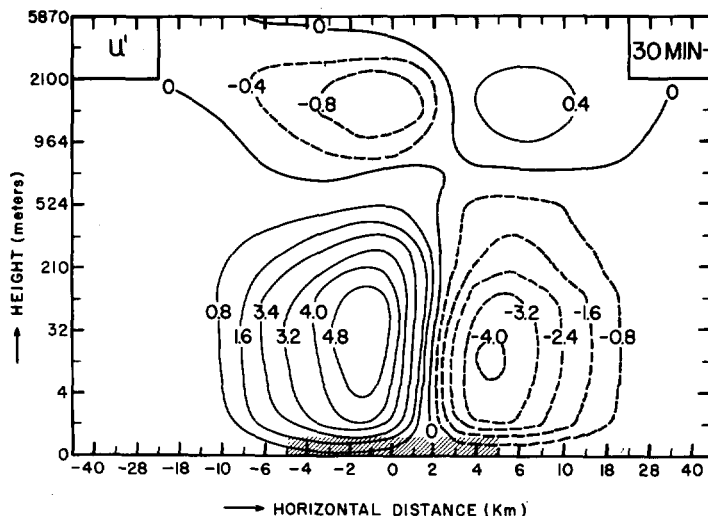


FIGURE 13.—Distribution of the horizontal perturbation velocity  $u'$  ( $\text{m sec}^{-1}$ ) at 30 min for case *a* when the initial prevailing flow is normal to the heat source.

the local acceleration is due primarily to the pressure gradient force. Further downwind of the heat source, at the point C, the local acceleration is mainly due to the horizontal advection of momentum.

At this juncture, it may be interesting to exhibit the perturbing effects of the heat source on the planetary boundary layer in greater detail. The effects are seen more clearly in figures 17 to 19 which show the  $x$ -variations of the perturbations in  $\theta$ ,  $u$ , and  $v$  at selected levels at  $t=3$  hr. The most striking impression one gets from these diagrams is that the heat source produces significant effects at considerable distances downwind. For example, the temperature perturbation pattern (fig. 17) shows an excess of as much as  $1^{\circ}\text{C}$  at a distance of about 20 km downwind from the leeward edge. The corresponding

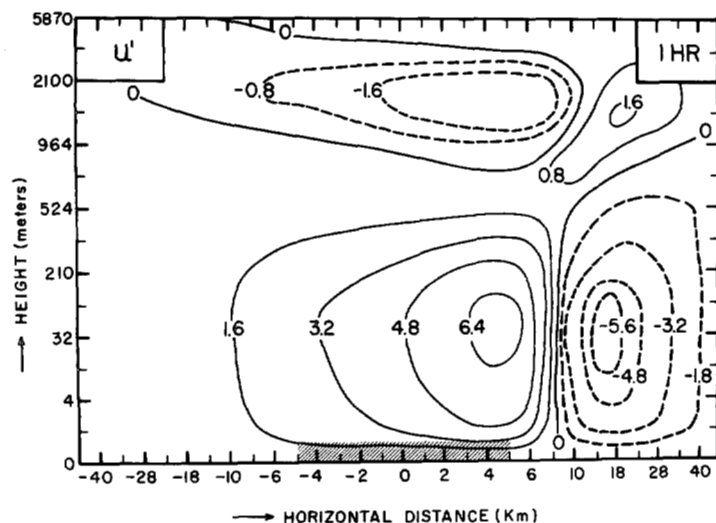


FIGURE 14.—Distribution of the horizontal perturbation velocity  $u'$  ( $\text{m sec}^{-1}$ ) at 1 hr for case *a* when the initial prevailing flow is normal to the heat source.

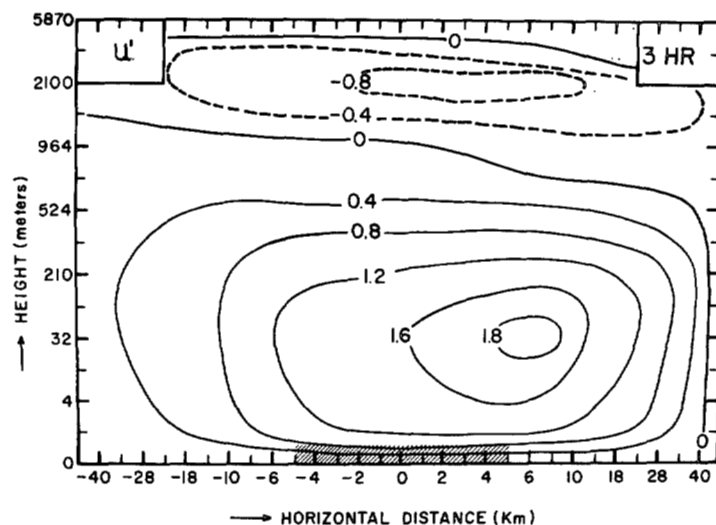


FIGURE 16.—Distribution of the horizontal perturbation velocity  $u'$  ( $\text{m sec}^{-1}$ ) at 3 hr for case *a* when the initial prevailing flow is normal to the heat source.

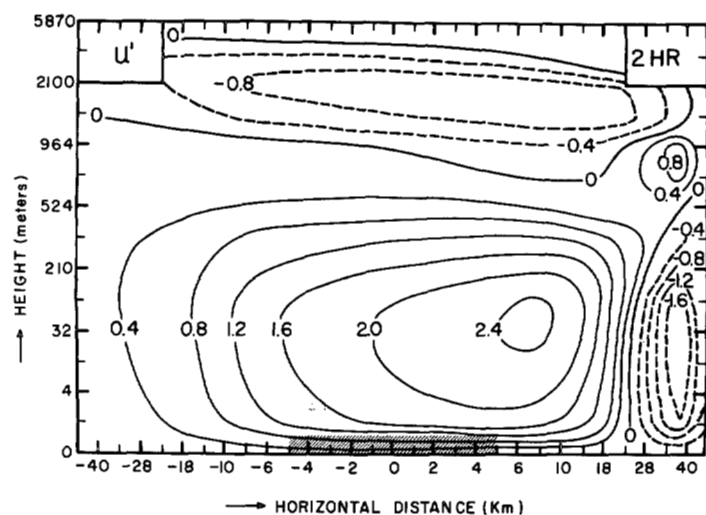


FIGURE 15.—Distribution of the horizontal perturbation velocity  $u'$  ( $\text{m sec}^{-1}$ ) at 2 hr for case *a* when the initial prevailing flow is normal to the heat source.

perturbation in the wind speed (fig. 18) at this distance is about  $1 \text{ m sec}^{-1}$ . These magnitudes in the perturbations appear to indicate that a relatively long fetch is required for flow patterns to achieve equilibrium with a new surface.

Interesting by-products of the computations are the fluxes of momentum and heat across the earth-air interface. Figure 20 shows the values at  $t=3 \text{ hr}$ . It will be remembered that the roughness parameter has been assumed to be uniform. Therefore, the horizontal variations in the fluxes are entirely due to the local heat source. The momentum flux shows the largest values over the heated surface. This is simply a reflection of the fact that the eddy diffusion is large over the central strip where the air is more unstable and is moving more

TABLE 2.—Magnitude of terms of local acceleration in  $u$  ( $\text{cm sec}^{-2}$ )

Location A (−5.0 km)						
Time (hr)	$u$ ( $\text{cm sec}^{-1}$ )	$-u \frac{\partial u}{\partial x}$	$-w \frac{\partial u}{\partial z}$	$-\frac{1}{\rho_s} \frac{\partial p}{\partial x}$	$+f\bar{v}$	$+ \text{mixing}$
0.5	714	−0.448	+0.029	+0.264	+0.002	+0.276
1.0	748	−0.208	+0.078	+0.214	+0.003	−0.117
1.5	687	−0.093	+0.007	+0.084	+0.004	−0.031
2.0	663	−0.063	+0.005	+0.079	+0.004	−0.029
2.5	654	−0.049	+0.004	+0.075	+0.005	−0.038
3.0	646	−0.043	+0.003	+0.062	+0.006	−0.036
Location B (+5.0 km)						
0.5	102	−0.019	+0.005	−0.312	+0.003	−0.207
1.0	1148	+0.291	−0.056	+0.651	+0.002	−0.989
1.5	831	−0.086	+0.004	+0.085	+0.003	−0.106
2.0	742	−0.039	+0.001	+0.056	+0.004	−0.046
2.5	712	−0.021	+0.001	+0.052	+0.004	−0.050
3.0	698	−0.028	+0.001	+0.050	+0.005	−0.035
Location C (+14.5 km)						
0.5	244	−0.030	−0.010	−0.205	+0.003	+0.040
1.0	−230	+0.049	+0.032	+0.061	+0.004	−0.423
1.5	640	+0.272	−0.058	+0.011	+0.004	−0.042
2.0	716	+0.049	−0.011	−0.015	+0.003	−0.031
2.5	696	+0.024	−0.004	−0.015	+0.004	−0.025
3.0	675	+0.027	−0.004	−0.023	+0.005	−0.011

rapidly. The heat flux curve shows the same trend. Large upward fluxes occur over the source, while downward fluxes occur over the outskirts. The maximum value of about  $6 \times 10^{-3} \text{ cal cm}^{-2} \text{ sec}^{-1}$  is approximately one-fifth of the solar constant.

*Parallel flow case (b)*—This describes the results for the case when the prevailing flow is parallel to the central strip. Here, we present calculated patterns only for

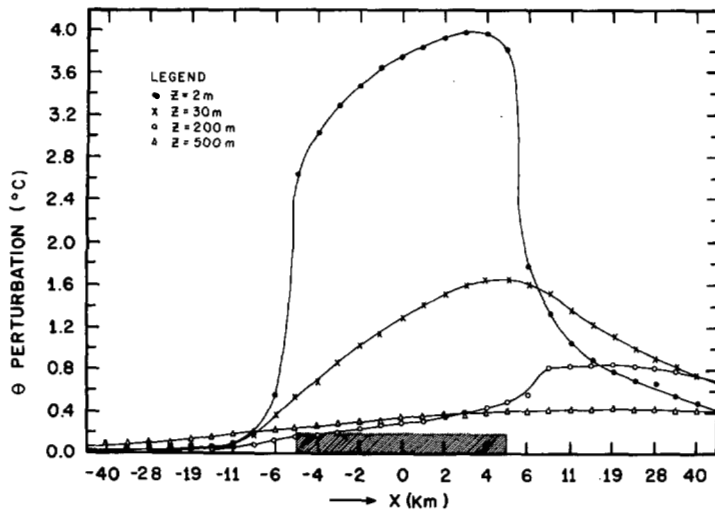


FIGURE 17.—Variation of perturbation in potential temperature along the  $x$ -direction at selected levels at 3 hr.

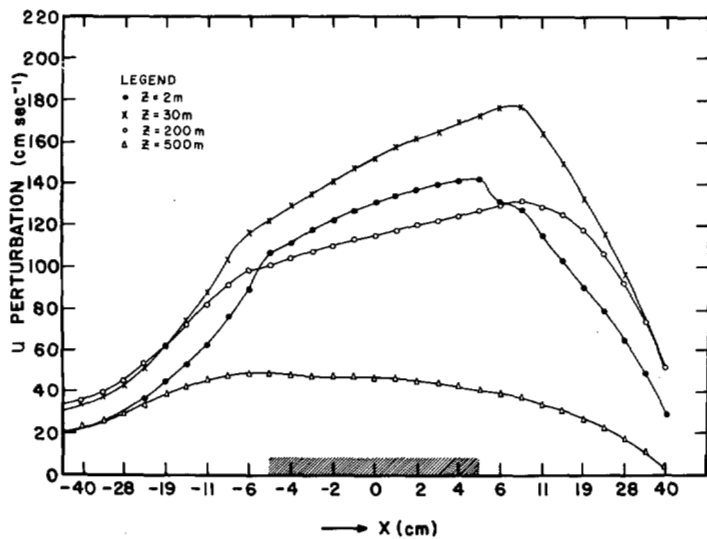


FIGURE 18.—Variation of horizontal perturbation velocity  $u'$  along the  $x$ -direction at selected levels at 3 hr.

temperature and vertical motion at  $t=15$  min, 1, and 3 hr after the initial time (figs. 21 to 27). As in the previous case, the isolines represent the excesses over the corresponding values (at the same level) at the upstream boundary. During the initial stages, the patterns are almost the same as in case  $a$ . Note, for example, the double cellular feature for vertical motion, one over each end of the heat source (fig. 21).

The most remarkable feature of the parallel wind case is the intensity of perturbations. At  $t=30$  min, the vertical velocity has a maximum value of  $1.2 \text{ m sec}^{-1}$  located right at the center of the central strip at a height of about 1.0 km. This value is  $1\frac{1}{2}$  times that for case  $a$ . The intensity increases to  $3.2 \text{ m sec}^{-1}$  at  $t=1$  hr. After this time, there

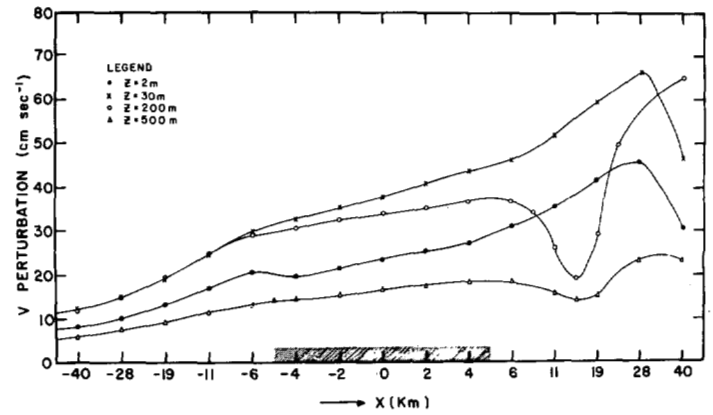


FIGURE 19.—Variation of horizontal perturbation velocity  $v'$  along the  $x$ -direction at selected levels at 3 hr.

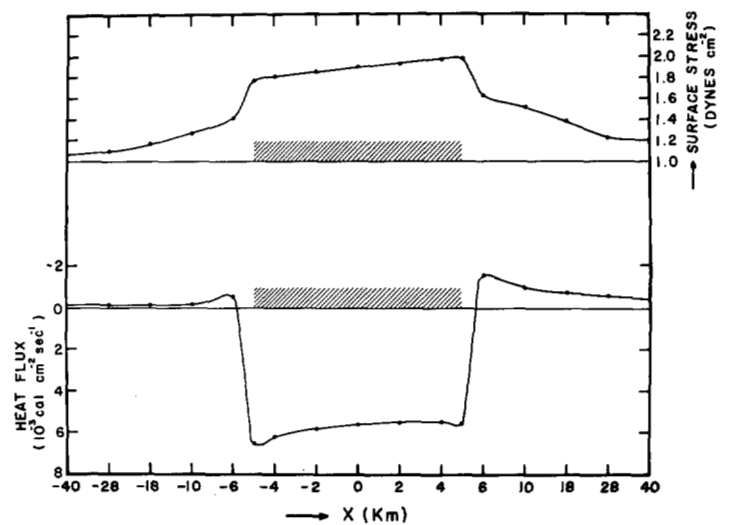


FIGURE 20.—Variation of the momentum flux and the heat flux along the  $x$ -direction at 3 hr.

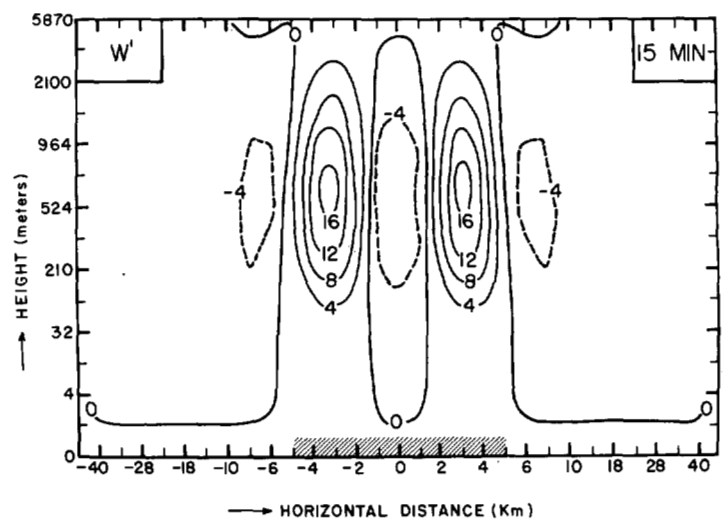


FIGURE 21.—Distribution of vertical perturbation velocity  $w'$  ( $\text{cm sec}^{-1}$ ) at 15 min for case  $b$  when the initial prevailing flow is parallel to the heat source.



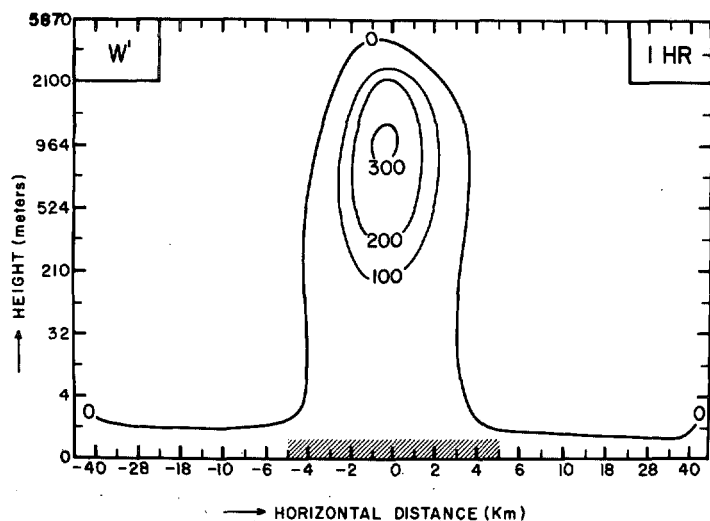


FIGURE 22.—Distribution of vertical perturbation velocity  $w'$  ( $\text{cm sec}^{-1}$ ) at 1 hr for case  $b$  when the initial prevailing flow is parallel to the heat source.

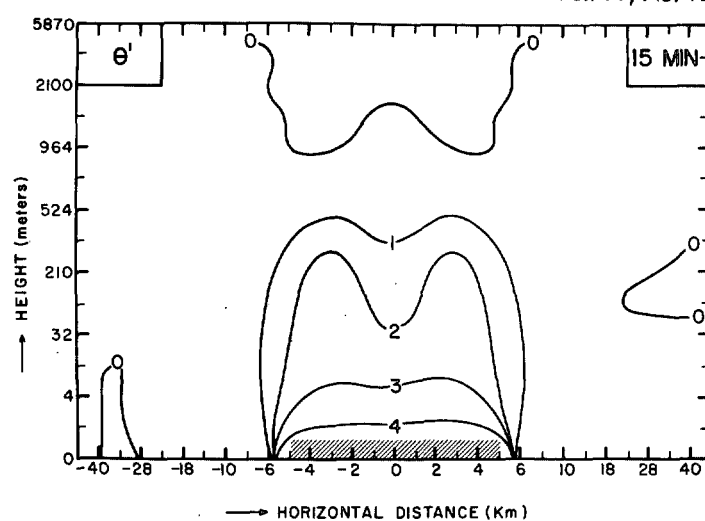


FIGURE 24.—Distribution of perturbation  $\theta'$  in potential temperature ( $^{\circ}\text{C}$ ) at 15 min for case  $b$  when the initial prevailing flow is parallel to the heat source.

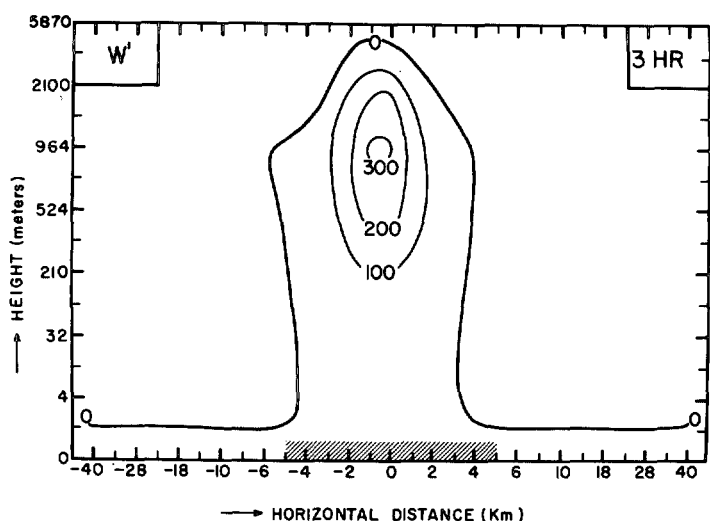


FIGURE 23.—Distribution of vertical perturbation velocity  $w'$  ( $\text{cm sec}^{-1}$ ) at 3 hr for case  $b$  when the initial prevailing flow is parallel to the heat source.

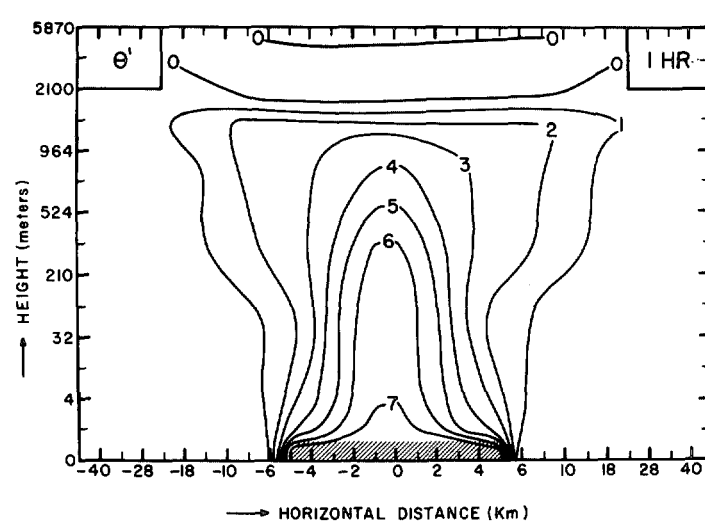


FIGURE 25.—Distribution of perturbation  $\theta'$  in potential temperature ( $^{\circ}\text{C}$ ) at 1 hr for case  $b$  when the initial prevailing flow is parallel to the heat source.

is very slight change either in the pattern or in the magnitude, indicating that almost a steady-state condition has been reached. The temperature fields show considerably more intense warming over the island in comparison with case  $a$ . As in the case of the velocity, the temperature patterns also show insignificant changes beyond  $t=1$  hr.

## 8. CONCLUSIONS

We have formulated a general model for studying the perturbing effects of a local heat source on the large-scale prevailing flow. An application of the model has been made to examine the development and approach to steady state of an induced perturbation under moderately strong

wind (without shear). In one case, the wind is normal to the heat source; in another case, the wind is parallel to it.

In the first case, the disturbance, which initially consists of two vertical circulation cells, develops into a single cell and approaches near steady state within a few hours. The descending arm of this circulation dominates over the entire extent of the heat source as well as the region upwind; the ascending arm is located downwind. Strong winds are induced in the surface layers over the entire central strip and the adjoining regions, both windward and leeward. The maximum surface winds occur over the leeward edge. The perturbation in the atmospheric boundary layer is significant up to a few tens of kilometers

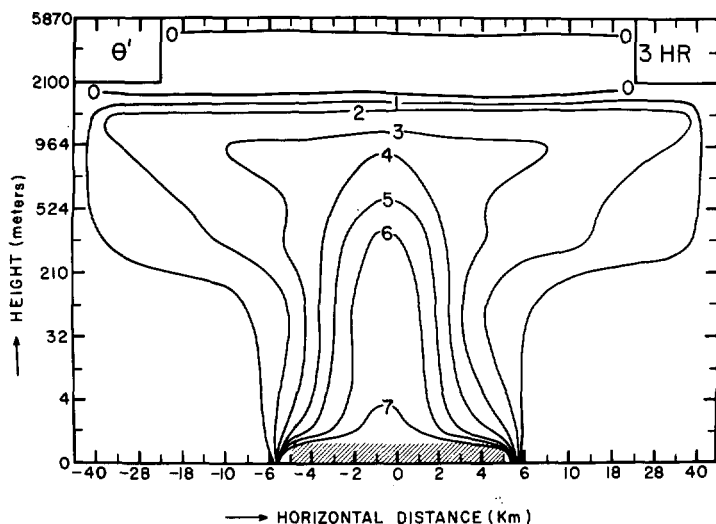


FIGURE 26.—Distribution of perturbation  $\theta'$  in potential temperature ( $^{\circ}\text{C}$ ) at 3 hr for case *b* when the initial prevailing flow is parallel to the heat source.

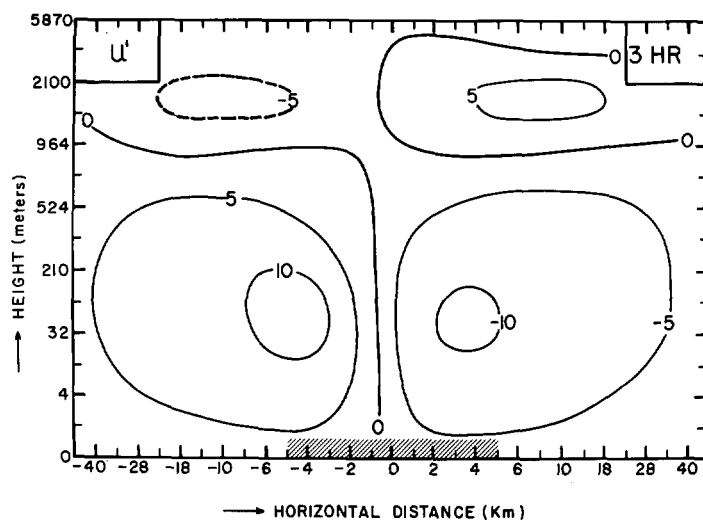


FIGURE 27.—Distribution of horizontal perturbation velocity  $u'$  ( $\text{m sec}^{-1}$ ) at 3 hr for case *b* when the initial prevailing flow is parallel to the heat source.

downwind. Above 1.5 km, the local heat source results in a deceleration of the flow. The apparent reversed sea-breeze effect on the leeward edge, indicated by our results, is a phenomenon which should occur only when the prevailing wind is strong. Integrations of a similar model showed that a regular sea-breeze-type inshore perturbation flow occurs if the prevailing flow is not greater than a few meters per second.

The second case (prevailing wind parallel to the heat source) shows features that are initially similar to those of the first case. However, with the passage of time, this case develops a much stronger perturbation; in this case, the maximum vertical velocity at  $t=3$  hr is about  $3 \text{ m sec}^{-1}$ . This value is approximately 100 times that for case *a*. This result shows that the intensity of the induced perturbation is small when the component of the prevailing wind, normal to the heat source, is strong.

The results of these preliminary calculations suggest possible further work. First, more integrations should be made in order to determine the characteristics of the induced disturbance as a function of the synoptic conditions, and the temperature of the island as well as its length. Second, the model equations should be formulated to incorporate variations along a third space coordinate. Third, the horizontal eddy diffusivity should be specified in terms of the large-scale flow parameters. Lastly, a model should include equations governing the microphysics of clouds and precipitation.

#### ACKNOWLEDGMENTS

The authors gratefully acknowledge the grant NSF GA-1492 that made this research possible. The computer facilities of the National Center for Atmospheric Research, Boulder, Colo., are deeply appreciated.

The manuscript was typed by Miss Marta Rivero.

#### REFERENCES

- Black, J. F., "Weather Control: Use of Asphalt Coatings to Tap Solar Energy," *Science*, Vol. 139, No. 3551, Jan. 18, 1963, pp. 226-227.
- Blackadar, A. K., "The Vertical Distribution of Wind and Turbulent Exchange in a Neutral Atmosphere," *Journal of Geophysical Research*, Vol. 67, No. 8, July 1962, pp. 3095-3102.
- Clayton, W. S., Texas A&M University, College Station, 1967, (personal communication).
- Estoque, M. A., "Vertical Mixing Due to Penetrative Convection," *Journal of Atmospheric Science*, Vol. 25, No. 6, Nov. 1968, pp. 1046-1051.
- Garstang, M., "The Role of Momentum Exchange in Flow Over a Heated Island," *Proceedings of the 1967 Army Conference on Tropical Meteorology*, Coral Gables, Florida, June 8-9, 1967, Report No. 15, Institute of Marine Sciences, University of Miami, Coral Gables, Fla., Jan. 1968, pp. 178-195.
- Lilly, D. K., "The Simulation of Three-Dimensional Turbulent Flow in Two-Dimensions," National Center for Atmospheric Research, Boulder, 1968, 7 pp., (unpublished manuscript).
- Lumley, J. L., and Panofsky, H. A., *The Structure of Atmospheric Turbulence*, Interscience Publishers, New York, 1964, 239 pp.
- Malkus, J. S., "Tropical Rain Induced by a Small Natural Heat Source," *Journal of Applied Meteorology*, Vol. 2, No. 5, Oct. 1963, pp. 547-556.
- Malkus, J. S., and Stern, M. E., "The Flow of a Stable Atmosphere Over a Heated Island—Part 1," *Journal of Meteorology*, Vol. 10, No. 1, Feb. 1953, pp. 30-41.
- Smith, R. C., "Theory of Air Flow Over a Heated Land Mass," *Quarterly Journal of the Royal Meteorological Society*, Vol. 81, No. 349, July 1955, pp. 382-395.
- Smith, R. C., "Air Motion Over a Heated Land Mass, Part 2," *Quarterly Journal of the Royal Meteorological Society*, Vol. 83, No. 356, Apr. 1957, pp. 248-256.
- Stern, M. E., and Malkus, J. S., "The Flow of a Stable Atmosphere Over a Heated Island—Part 2," *Journal of Meteorology*, Vol. 10, No. 2, Apr. 1953, pp. 105-120.

[Received February 24, 1969; revised June 27, 1969]